JOINT EUROPEAN TORUS JET

JET–P(87)60

A.P.H. Goede, B.R. Nielsen, F. Shone, T.Sønderskov
and E. Thompson

Engineering, Manufacture and Test of the Deflection Magnets of the JET Neutral Beam Injector

Engineering, Manufacture and Test of the Deflection Magnets of the JET Neutral Beam Injector

A.P.H. Goede[1], B.R. Nielsen[2], F. Shone[3], T.Sønderskov[2] and E. Thompson[1]

JET-Joint Undertaking, Culham Science Centre, OX14 3DB, Abingdon, UK

[1]JET-Joint Undertaking, Culham Science Centre, OX14 3DB, Abingdon, UK
[2]Danfysik AIS, 4040 Jyllinge, Denmark
[3]AEA Risley, Warrington, WA3 6AT, UK

Preprint of Paper to be submitted for publication in
Nuclear Instruments and Methods in Physics Research, Section A

ABSTRACT.

The engineering design, the manufacturing methods and the magnetic measurements of the ion deflection magnets of the Joint European Torus (JET) Neutral Injection system are described. The magnets are ultra-high vacuum compatible, the coil being encased in a stainless steel jacket which incorporates a highly optimised water cooling system. High emphasis is placed on the reliability of the system. Magnetic measurements show adequate agreement with 3D computations and time dependent eddy-current computations.

1. INTRODUCTION

The JET (Joint European Torus) neutral beam injection system delivers additional heating power to JET by injecting neutral atom beams of hydrogen or deuterium into the Tokamak plasma [1]. One of the two presently installed injection systems has been operated with 80 keV deuterium beams delivering a total neutral beam power of 10 MW for several seconds pulse length to the plasma [2]. The injection systems are designed to be upgraded to 160 keV D° operation. The deflection magnets serve to separate the non-neutralised ion beam fraction from the beams after extraction and neutralisation. The safe handling of this large amount of ion power (up to 26 MW) necessitates a careful magnet design.

The magnets are designed to meet the following special requirements:

- Vacuum compatibility. The magnets are completely immersed in the ultra-high vacuum system of the injector.
- High reliability (10^5 pulses). The high operation costs of JET do not allow extensive down time.
- Compactness. The severe spatial constraints inside the injector box require a slim coil design and efficient iron circuit.
- Limited radiation resistance (< 10^8 Rad). This is required during the tritium operation phase of the project.

A unique feature of the engineering design is that the coil and its vacuum enclosure form one integrated unit, which incorporates a highly optimised water cooling system with an internal water manifold. This has resulted in a compact coil design with a low risk of water leak inside the vacuum system.

To date two magnet systems have been commissioned successfully, with a third (spare) set of magnets under manufacture (1987). A photograph of the completed assembly is shown in Figure 1. The first magnet system has operated successfully for 5000 neutral injection pulses at modest excitation level. The second system has run routinely for over 500 pulses at the maximum design specification required for 160 kV deuterium operation.

In this paper we shall describe the engineering design of the magnets, the manufacturing procedures and tests and the magnetic field measurements which are compared with 3D computations. The physics design of the magnet, in particular the ion-optical calculations are reported in a separate paper (3, 4).

2. MAIN PARAMETERS

A schematic diagram of the magnets is shown in Figure 2. It represents one quadrant of the total system in which four magnets deflect the beams of 8 ion sources. The iron circuit of two vertically adjacent magnets is symmetric around the midplane (horizontal-axis in Figure 2) and is magnetically coupled through a common inner return yoke. Two such magnet pairs are mounted on either side of a central support column. This column also serves as a support for the beam dumps and the calorimeter and acts as the main water supply line. The whole system is inserted into a 7 m high, 3.5 m long vacuum box.

The basic magnet parameters are listed in Table 1. They follow directly from the physics parameters, ie. the bending angle and the gap width required. A 90° bending angle for 160 keV D^+-ions defines a magnetic field line integral of ~ 0.12 Tm. This number may be obtained by either increasing the magnetic field strength or the magnet dimensions and these parameters require optimisation. The length of the magnet was limited by the overall length of the injector (which is kept short in order to minimise beam transmission losses), and by gas pumping requirements (in order to minimise beam charge exchange losses inside the magnet). On the other hand, the maximum attainable field is set by saturation in the iron of the yoke for which the dimensions are restricted. As a result of this optimisation process, a magnetic field strength of ~ 0.2 T was selected.

The gap width needs to be consistent with good beam transmission. There is a premium on minimisation of the gap width as it allows maximum dimensions for the iron circuit within a constant space envelope, and it reduces the number of ampère turns and thus the iron dimensions required. A gap width of 22 cm was chosen, allowing 1.5 cm on each side of the beam for water-cooled pole-face liners. Allowing for unavoidable saturation in the iron circuit this yields a number of ampère turns of approximately 2×10^4 per coil.

The number of ampère turns may be obtained either by current or by number of turns and this is largely determined by power supply and power transmission considerations. At JET the distance between power supply and magnets is about 70 m and clearly cable losses will be

significant at large currents. Also inside the injector the transport and vacuum feedthrough of the current is much simplified if water cooling can be avoided. After optimisation of the coil cooling circuit (Section 3) a coil of 24 turns (8 x 3) was chosen operating at 833 A nominal current.

The iron circuit is of the picture frame type. The coils are positioned approximately flush with the pole-face surface in order to maximise the magnet efficiency. This also produces a sharp field boundary which is important to avoid penetration of the magnetic field into the neutraliser and thus cause beam loss. The minimum dimensions of the iron circuit are bound by saturation, the critical region being the iron thickness above the coils which carries half of the total gap flux. Because of space limitations a degree of saturation had to be accepted in this region. For the inner return yoke, positioned at the horizontal plane of symmetry (horizontal-axis in Figure 2),and where the dimensions are limited by the spacing of the neutral beams, the problem of saturation was overcome by a magnetic coupling of the two vertically adjacent magnets through a common inner return yoke. This makes use of the fact that the return fluxes of the two adjacent magnets cancel. The remaining iron thickness is sufficient as to allow a limited variation in excitation of each magnet and thus beam energy from quadrant to quadrant.

Two-dimensional computational studies were carried out to obtain an accurate prediction of the fringe field distribution and to establish the level of saturation in the iron circuit in order to optimise the

dimensions of the iron circuit and the coil current. Also, the effects of coil shape and position and the effect of field clamps were investigated (field clamps are extensions of the iron circuit overhanging the coil at the entrance and exit apertures). Field clamps were found to produce a more rapid fall-off of the fringe field. At the same time, however, they create a negative undershoot in the field, the combined effect of which leads to the requirement of an increased number of ampère turns and an extended low level magnetic field which penetrates further into the neutraliser. Therefore, this option was rejected. The most sensitive shape parameter of the fringe field was found to be the distance between the coil and the pole face. This distance was minimised in order to create a sharp field boundary.

The two-dimensional studies and the first three-dimensional study were carried out [5] employing the magnetic field code GFUN [6]. Final optimisation was performed by JET using the TOSCA-3D code [7].

3. ENGINEERING DESIGN

3.1 Iron circuit

The iron circuit is fabricated from low carbon iron (< 0.01%), which was forged and heat treated (Röchling AME2SX1). This quality of iron has a substantial permeability even at the high magnetising fields prevalent in the circuit ($\mu \approx 200$ at $B \approx 1.8$ T). Also, the coercive force is low (50 A/m) reducing hysteresis and remnant magnetism in pulsed operation. The forged quality of iron is specified in order to

minimise voids and laminations. The circuit is built up from solid iron slabs rather than laminated sheets for vacuum considerations. The entire iron circuit is electro-chemically nickel plated in order to reduce surface gas desorption (Kanigen process, layer thickness 25 μm).

The iron circuit forms the structural element of the magnet, capable to take the bending stresses induced on the poleslab by the magnetic field (≤ 0.3mm deflection) and the stresses transferred from the coils, which are fixed to the sides of the poleslabs by means of brackets. The differential stress induced by the radiation cooling of the poleslab facing the cryopumps is shown to be small because of the high thermal conductivity of the iron circuit. The iron circuit also serves as the mechanical support for the pole face liners and the fractional energy dumps . The poleface liners are simple edge cooled copper plates bolted on to the polefaces by low heat-transfer connections and clamped at the edge to stainless steel water pipes to provide cooling during the off-duty period. They act as beam defining scrapers and as intercepting plates for the fractional energy ions. Most of the fractional ions are collected by the fractional ion dumps which are mounted from the magnet return yokes. These dumps employ the same high heat transfer cooling technique as used elsewhere in the injector. With their water cooling circuit incorporated in the magnet assembly, the magnet liners and fractional energy dumps form a single modular unit for assembly on to the central support column. This is an essential aspect of the design in view of the remote handling requirement envisaged for the active phase of JET.

3.2 Coil

Each coil consists of 24 turns of hollow copper conductor (OFHC annealed copper), water-cooled, which are arranged in 8 concentric subcoils connected electrically in series and hydraulically in parallel. The windings are insulated by glass reinforced epoxy with a polyimide (Kapton) layer between the outer conductor and the stainless steel can which is at earth potential. The coils and water manifolds are encased inside a stainless steel can. Water pipes and current leads are fed through the can separately, using a metal to ceramic insulator for the current leads and an internal cast epoxy insulator for the water manifold. After the closing weld of the can the entire assembly is vacuum impregnated with epoxy for the second time, creating a monolytic can-coil entity. The extensive manifolding made it possible that the sub-coils could be wound from a continuous length of conductor (~ 17 m), thus avoiding the need for internal brazed joints.

A cross-section of the canned coil is shown in Figure 3a. The closing weld of the two U-sections of the can is performed along the neutral line of the assembly to avoid weld distortion. The nominal space between coil and can is 3 mm. In order to protect the epoxy insulation from overheating during the closing weld, a 50% penetration butt-weld is used, shielded on the inside by a sandwich of stainless steel (0.3 mm to avoid weld corrosion), glass tape (0.2 mm for thermal insulation) and copper (0.15 mm adjacent to the coil to spread the heat). The copper strip is discontinuous to avoid short circuit. A prototype can was manufactured to establish the optimum welding sequence and to prove that a helium leak-tight can could be produced within the dimensional tolerances.

The lead-through section, shown in Figure 3b, proved to be one of the more complex aspects of the design. An important design principle adopted was the use of exclusively stainless steel TIG-welded joints for all external vacuum interfaces of the can, in order to provide a reliable solution against vacuum leaks and outgassing. By choosing large section copper rods for the current feedthroughs, which are conduction and radiation cooled, the cooling water could be led through the can separately by stainless pipes. The insulator to can interface contains an external welding lip (6) which allows for separate dismantling of the feed through section.

The water-manifolds and the current feedthroughs are mechanically connected to the can through a flexible bellows section (single-wall stainless steel 304 L). The bellows (4) of the current lead serves to accommodate mechanical tolerances during the assembly of the conductor in the ceramic to metal seal, which must not be subjected to mechanical stress. The bellows (10) of the epoxy water manifold serves to accommodate the shear stresses that occur during the curing phase of the second impregnation process. They are padded (8) with a silicon foam (Dow Corning 03-3321) to provide a flexible interface with the glass epoxy. In contrast, the bellows of the electrical feedthrough is entirely filled with epoxy during the second impregnation phase, in order to avoid the occurrence of Paschen breakdown. Here differential expansion coefficients are minimal. Care was taken to support all the epoxy volumes in the feedthrough housing by glass fibre reinforcements.

A salient feature of the design is that it allows for a sequential testing sequence at each stage of manufacture thus adding a further safety barrier against malfunction. After the coil impregnation before canning, the coil manifold assembly is subjected to hydraulic tests (20 bar) and high- voltage insulation tests (5 kV AC, 2 kV DC), the latter after a 24 hr water immersion cycle. Subsequently, after canning but before the second impregnation, the coil and can are helium leak-tested and subjected to further high-voltage and hydraulic tests. Finally, after the second impregnation the high-voltage and hydraulic tests are repeated again. The successfulness of this procedure may be illustrated by the fact that one of the coils, installed adjacent to the cryopumps, survived a water freeze-up accident after loss of waterflow in stand-by.

3.2.1 Coil insulation

The insulation system of the coils consists of glass and polimide (Kapton) tape, vacuum impregnated with epoxy resin, similar to the system employed on JET for the toroidal and poloidal field coils [9]. The insulation thickness is 1 mm in between turns, consisting of half lapped glass tape only, and 2 mm for the outer to ground layer containing an interleaved Kapton layer. Similar to the procedure specially developed for JET [10], a flexibiliser (5% CIBA-DY040) was added to the resin system, in order to ensure a good bond to the Kapton film. Furthermore the copper conductor is glass-bead blasted and coated with a primer (CIBA-DZ80) in order to improve the epoxy to copper adhesion. The maximum shear strength thus obtained is 33-46 N/mm^2 and is limited by the insulation matrix not the bond strength between copper and insulation. The resin system for the first

impregnation stage consists of araldite CIBA-MY750 with hardener HY906 and accelerator DY073. For the second impregnation stage the hardener was changed to HY905 to allow curing at lower temperatures (about 105°C) to limit thermal stresses.

In a separate investigation the radiation resistance of an epoxy sample (mechanical properties) was shown to allow radiation exposure in excess of 10^9 Rad well within the maximum expected JET dose of 10^8 Rad.

Impregnation is carried out in a rigid pressurised steel mould, which defines the final coil dimensions. The mould is designed for the simultaneous impregnation of two mirror image coils in order to speed up production. The impregnation temperature of the system is 55°C ± 5°C at 0.5 torr pressure, the curing temperature 155°C. During the second impregnation the can and the coil are heated by passing current through the coil and by heating tapes and thermal insulation wrapped around the can. During curing the can is rigidly clamped to a baseplate to avoid distortion. Three small ports in the can for pumping a filling are welded up as the final step in the canning procedure.

3.2.2 Watercooling system

The main constraint for the coil cooling arises from the limited water pressure drop of 1.7 bar available from the central support column, which supplies the water cooling to all the internal components of the injector box, such as the ion dumps. The large flow this requires (500 ℓ/s) makes a low pump driving pressure essential [1].

A number of coil winding geometries were analysed with the objective to minimise the coil temperature rise, taking into account the dimensional constraints of the coil cross-section and in particular its height. The maximum temperature rise allowed is set by the maximum internal shear stress and the deflection temperature of the epoxy system (~ 105°C). For the high Reynolds-number flow considered here, the film temperature drop between the copper and the water is small. Thus, the coil temperature is essentially equal to the bulk water temperature. Active cooling is required because the JET pulse sequence is too long ($\gtrsim$ 60 sec, incl. pre-pulse checks) to rely on the thermal inertia of the coils with cool-down in the off-duty period.

The temperature rise of the coil is determined by the following factors: the number of ampere turns defining the magnetic field strength, the resistivity of the conductor, the characteristics of the coolant, the water pressure drop, and a geometry factor. Only the latter permits optimisation. It can be shown that this geometry factor has the following dependence on temperature.

$$(\Delta T)^{-1} \propto n_1^{2}\, n_2^{3/7}\, a^{33/7} \left(\frac{d}{a}\right)^{19/7} \left\{1 - \frac{\pi}{4}\left(\frac{d}{a}\right)^{2}\right\} \qquad (1.)$$

where n_1 = number of subcoils hydraulically separate,

n_2 = number of turns in one subcoil,

a = outside dimension conductor,

d = dia. cooling channel.

A square section conductor profile is assumed for maximum filling factor.

A similar formula can be derived for the film temperature drop with slightly different values in the exponents. It is immediately clear that by increasing the number of parallel cooling circuits (n_1) at constant number of ampere turns ($n_1 x n_2$) the temperature rise is reduced. The conductor size should be maximised, consistent with the given number of turns and overall dimensions. The conductor bore size is optimum at a ratio d/a = 0.856. The expression for the film drop yields a slightly lower value (0.72) for this parameter. However, in both cases a fairly broad maximum exists (± 10% variation) in the range $0.65 < d/a < 0.9$. In order to minimise the electrical power requirements a d/a value at the lower end of the range is favoured.

An analysis of a large number of coil geometries (30), making use of commercially available conductor profiles, resulted in the selection of a system of separately cooled subcoils, arranged in concentric cylindrical shells rather than pancakes. This arrangement minimises internal thermal stress and avoids thermal short circuits. The maximum number of subcoils is limited by the space available for manifolding to eight. With three turns stacked vertically the coil height was minimised, whilst the increased coil width could be accommodated. The water inlet of a sub-coil was chosen to face the magnet aperture, which tends to bend the coil away from the transmitting beam when heated. Details of the selected coil parameters are given in Table II.

During the magnet test program the measured temperature rises of the coil and the outlet water showed good agreement with the calculations (here a film temperature drop of ≈ 2°C must be added to the bulk temperature rise calculated by Eq.1). From Eq.1 it follows that an

enhanced cooling power ($\Delta T \approx 24\%$ lower) could have been achieved with a 6 mm bore cooling channel in an otherwise identical geometry, at the expense of a higher electrical power (+ 25%). However, as the thermally induced shear stresses in the coil stay within acceptable limits for the geometry selected, the slightly smaller cooling channel was favoured with the aim to reduce power requirements.

Thermally induced shear stress in a metal-epoxy-metal sandwich may be calculated analytically by considering the elasticity equations and by applying the equilibrium conditions for stress and strain at the metal to epoxy interface [11]. The shear stress in the epoxy for a sandwich which is long in relation to its width is given by:

$$\tau = \alpha \Delta T \left\{\frac{aGE}{2h}\right\}^{\frac{1}{2}} \qquad (2)$$

where τ = shear stress insulation

α = thermal expansion coefficient of copper = 16.7×10^{-6} $°C^{-1}$

$\overline{\Delta T}$ = temperature difference of metal layers = 35/3 °C

a = dim. copper winding = 8 mm

h = insulation thickness = 1 mm

G = shear modulus epoxy = 3×10^3 N/mm^2

E = Elasticity modulus copper = 1.18×10^5 N/mm^2

For the above numerical values this yields a shear stress $\tau = 0.628\ \Delta T = 7.3$ N/mm^2, which is well below the maximum shear strength of the epoxy-glass matrix (33 - 46 N/mm^2).

3.3 Ancillary Systems

3.3.1 Busbar System and Vacuum Feedthroughs

Inside the Neutral Injector vacuum box the current to the magnets is supplied by a radiation-cooled busbar system. The busbars are surrounded by a plasma-tight shield to prevent electrical breakdown. The system is rated for continuous operation, the emissivity of the copper being enhanced to 0.3 by glass-bead blasting and the aluminium shield being black anodised using the same dye as used for the cryopumps (Sanodal MLW), yielding an emissivity value of 0.96. The busbars are suspended from a support structure by metal to ceramic insulators and mechanically fixed at one point to allow for thermal expansion. The interface to the magnets and vacuum feedthroughs is through braided wire cable (wire dia 0.1 mm, total copper area 500 mm^2) crimped onto lugs that are EB welded on the busbars (15 x 75 mm^2). The braided cable is outgassed at 700°C in hydrogen atmosphere before crimping.

3.3.2 Power Supply

The acceptance of the ion dumps allows a magnetic field variation of approximately ± 1%. Hence a simple multiphase rectified, thyristor controlled power supply was acceptable to power the magnets. Protection and interlock of the magnets has to be compatible with the vacuum and radiation environment of the magnets which rules out Hall probes. A simple over/under-volts limit and Wheatstone bridge comparator arrangement of the two coils of one magnet was chosen to

protect the coils against shorted turn and/or loss of coolant. The most important interlock between magnet current and beam extraction voltage is provided by a fail-safe real-time comparison of both parameters. Timing, current setting, check and all other control functions are performed remotely by the JET CODAS computer control system.

4. MAGNETIC MEASUREMENTS

4.1 Field Mapping

A detailed mapping of the magnetic field was carried out and compared with the TOSCA-3D computer predictions. Measurements were carried out with 3D-Hall probes fixed on a carriage moved along by stepping motors, controlled and processed automatically. Typical results are shown in Figure 4. In the median plane (Figure 4a top) the agreement with the absolute value of the magnetic field strength is within 1.5%. The position of the effective field boundary is found to be further inward by up to 2%. Both effects produce a reduction in the actual bending power by up to 3.5% in hydrogen and up to 1% in deuterium operation, which can be compensated for by adjusting the coil current. The reversal of the fringe field due to saturation at high fields (Figure 4c) is not as strong as predicted, resulting in a closer resemblance of the hydrogen and deuterium operation modes.

Measurements made in a plane near the poleface, 8 cm off the median plane, show a profile that is less steep than calculated (Figure 4a bottom). This effect shows up more pronounced in the field components parallel to the poleface (Figure 4b). The field integral of these

planar components is, in some cases, smaller by up to 9%, but this is partially compensated by the higher magnet current required as discussed above. Consequently, the vertical focussing produced by these components is slightly weaker than predicted.

The remnant magnetic field strength is about 4 G in good agreement with the calculations. The reproductibility of the magnetic field strength (incl. hysteresis), its symmetry around the median plane, and the variations from magnet to magnet are all within 0.2%.

In conclusion, the accuracy of the TOSCA-3D predictions has been adequate for our purpose. In the fringe field, the predictions are generally less accurate, which shows up in the oscillations of the main field components (Figure 4a bottom) and the discreetness in the calculation of the planar field components (Figure 4b). We were unable to resolve these computational artefacts with the available codes.

4.2 Eddy-Current Calculations

As a consequence of the choice of a solid iron yoke, the dynamic behaviour of the magnets is governed by eddy-currents. In pulsed operation this leads to relatively long rise-times of the magnetic field (much longer than the inductive time-constant) which may become incompatible with the overall JET timing sequence. To assess this problem, a 2D time-dependent computation was carried out, using the PE2D-code [8], which takes into account the finite and non-linear permeability of the iron. The following phenomena could be observed; during the current-ramp high eddy-currents are first generated in a

thin iron layer around the coils limiting field penetration. Subsequently, the flux spreads out in a narrow layer around the gap and forces this part of the iron into saturation, thus locally reducing the permeability of the iron. As a result the field penetration time, given by $\tau = \mu d^2/\rho$ is much shorter than the steady-state permeability of the iron would suggest (μ = magnetic permeability, ρ = resistivity of the iron, d = skin depth). After about 14 sec the final field distribution is established in those parts of the iron circuit that are already saturated during steady-state. Since those parts dominate the reluctance of the circuit, the field in the air gap is also close to its final value (~ 99%) after 14 secs. The central part of the iron-circuit, however, is still far from equilibrium. This is reached only later than 75 sec, a value in better agreement with the skin depth formula applied to the unsaturated bulk of the iron, but not important for our application.

Measured rise times (99% level) in the centre of the magnet are 3.7 sec for I_M = 736 A (160 kV deuterium operation) and 6.1 sec for I_M = 291 A (80 kV hydrogen operation) respectively, where I_M is the magnet current. These times are independent of current rise time. Rise times are shorter for high field operation and similarly they are slightly shorter near the coils, consistent with the higher saturation levels existing in the iron. The discrepancy between the PE2D-code (14 sec rise time) and the measured value (3.7 sec rise time) is attributed to the two-dimensional nature of the computations which ignores field penetration from the sides of the magnet (ie. the code assumes the short dimension of the magnet to be infinitely long). In addition the

effect of small airgaps in between the various parts of the iron circuit was not modelled and this increases the effective resistivity of the iron and hence the flux penetration time. The above rise times turn out to be of the same magnitude as other lead times in the count-down of the JET pulse and thus allowed the magnets to be incorporated in the JET timing sequence.

5. Conclusion

The canning of the coil in a stainless steel jacket, incorporating the water manifolding system, and completely impregnated with epoxy to form a monolitic entity, has offered a reliable and compact design solution for an ultra-high vacuum compatible magnet system, employed for the JET neutral injection system. The design calculations presented in this paper concerning the mechanical stress, the heat transfer and the magnetic field were essential in obtaining an optimised design. Their predictive qualities have been shown to be in good agreement with the measurements and the operational experience gained so far.

Acknowledgements

We would like to thank Dr J H Coupland of Rutherford Laboratory and Dr P H Rebut, J R Last, J Booth and P Doidge of JET for their advice and their useful ideas in the design of the magnets.

References

[1] G Duesing, H Altmann, H Falter, A Goede, R Haange, R S Hemsworth, P Kupschus, D Stork, E Thompson, Fusion Technology 11, 163 (1987).

[2] A P H Goede, C Challis, T T C Jones, A Stäbler, D Stork, E Thompson. Proc. 14th Symp on Fusion Technology, Avignon (1986) Pergamon Press (1986) Vol 2, 1139.

[3] A P H Goede, A A Ingersoll, P Kupschus, B R Nielsen, E Thompson, R S Hemsworth, Proc 12th Symp Fusion Technology, Jülich, FRG, Sept 1982, p.1321, published for the Comm of European Comm by Pergammon Press (1983).

[4] A P H Goede, B R Nielsen, E Thompson, to be published

[5] D E Baynham, J H Coupland, T C Randle, Rutherford Lab report RL-81-060 (1981).

[6] M J Newman, C W Trowbridge, L R Turner, Proc 4th Int Conf Magnet Technology, Brookhaven (1972).

[7] J E Simkin, C W Trowbridge, IEEE Proc 127, 368 (1980).

[8] C S Biddlecombe, J E Simkin, Rutherford Lab report RL-79-089/Rev.2

A G Armstrong, C J Collie, J E Simkin, C W Trowbridge, 2nd Int Conf on Computing Magnetic Fields COMPUMAG2, Grenoble (1978).

[9] M Huguet, K J Dietz, J L Hemmerich, J R Last, Fusion Technology 11, 43 (1987).

[10] J R Last, A Bond, E Salpietro Proc 10th Symp on Fusion Technology, Padua, Italy, (1979) p.1025, published for the Comm European Comm by Pergammon Press.

[11] J R Last Internal JET design note JGN E(76) 2.

TABLE I	
Magnet Parameters (One Quadrant)	
Magnetic Field strength (T)	0.1798
Ampère turns (A)	24 x 833
Gap width (cm)	22
Gap length x height (cm^2)	~100 x 200
Power consumption (kW)	74
Outside dim coil can (mm^2)	38 x 86
Pole slab thickness (mm)	120 (86 above coil)
Weight of one quadrant (kg)	3500

TABLE II	
Coil Parameters	
Windings ($n_1 x n_2$)	8 x 3
Current (A)	833
Electrical resistance (mΩ)	53
Conductor dim (mm^2)	8 x 8
Cooling channel dia (mm)	4.9
Cooling channel length (m)	17.1
Current density (A/cm^2)	1881
Filling factor can assembly	0.33
Water pressure drop (bar)	1.7
Water flow per coil (ℓs^{-1})	0.26
Water velocity (m/s)	1.65
Reynolds number	1.07×10^4
Temp rise water	
calculated (°C)	35°
measured (°C)	32°
Temp rise time 80% meas.(sec)	~60

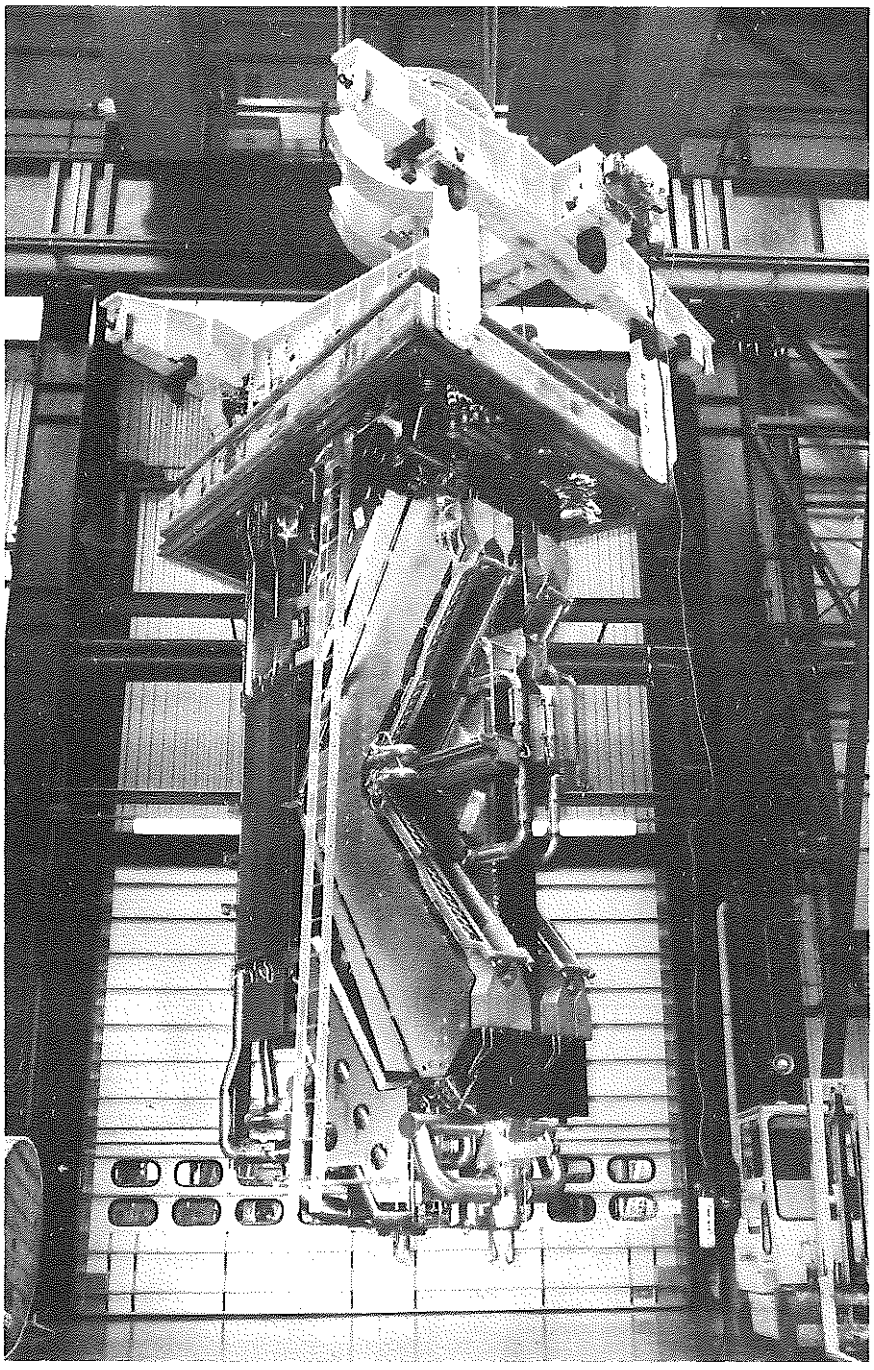

Figure 1 Photograph of the central column mounted inside the JET neutral particle injector.. The four magnets on the column deflect the non-neutralised ion beam fractions extracted from eight ion sources, and deflect these on four ion dumps comprising a total power of 26 MW. At the magnet exit a movable calorimeter door measures the neutral atom beam fraction. All major components are actively cooled by a 500 ℓ/s water supply incorporated in the column. The entire system, $\sim$ 7m high and $\sim$ 35 tons in weight, is inserted in the injector vacuum box.

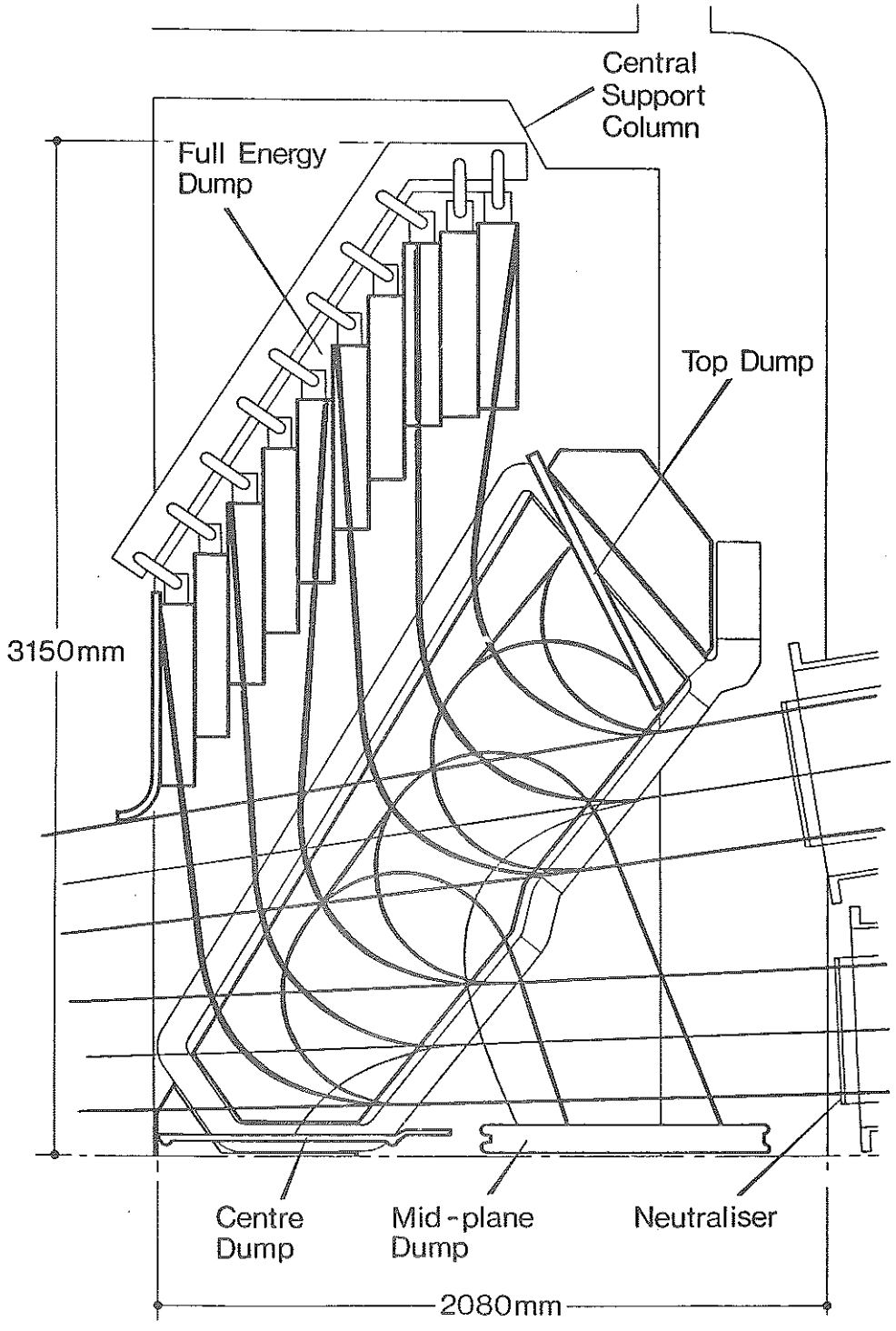

Figure 2 Schematic of JET neutral injector deflection magnets (one quadrant shown). Each magnet deflects the ion beam fraction of two ion sources. Sample ion trajectories of the full energy ion components (80 KeV hydrogen, 160 KeV deuterium) and the fractional energy ion components (molecular break-up products) are shown.

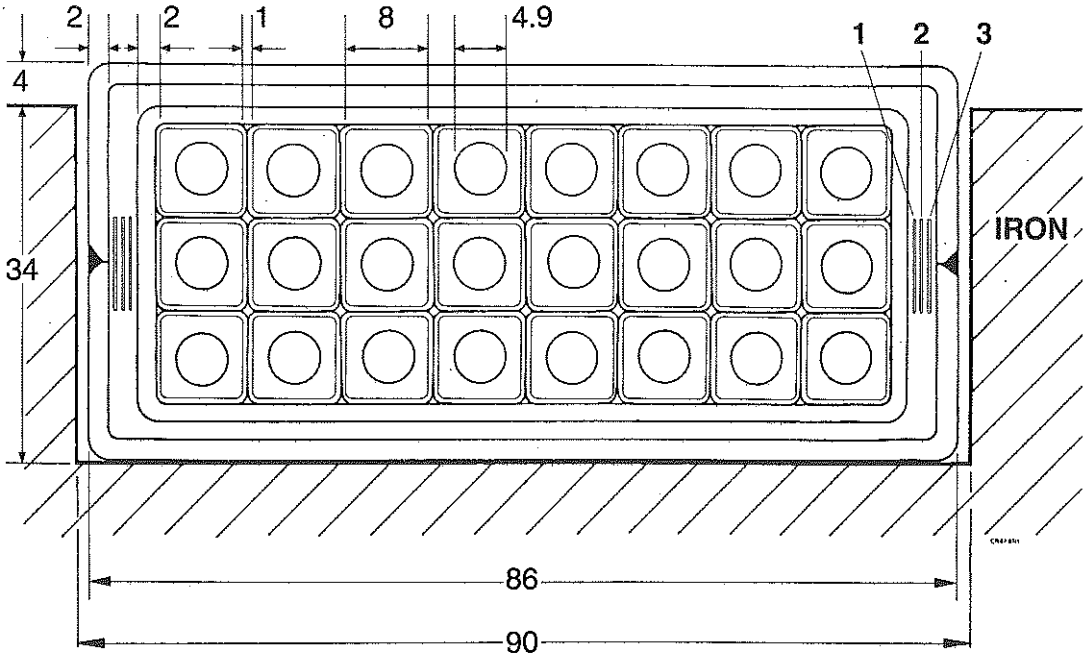

Figure 3a Cross-section of the magnet coil. The coil is wound from OFHC copper profile of 8 x 8 mm^2 with a 4.9 mm cylindrical cooling channel. Glass-epoxy insulation thickness is 1 mm in between windings and 2 mm for the outer to ground layer. The stainless steel vacuum enclosure (2 mm wall thickness) is separated from the coil by a SS (3), glass (2), Cu (1) sandwich to protect the coil against overheating during the closing weld. The interspace between can and coil is subsequently filled with epoxy to form a monolytic coil-can assembly.

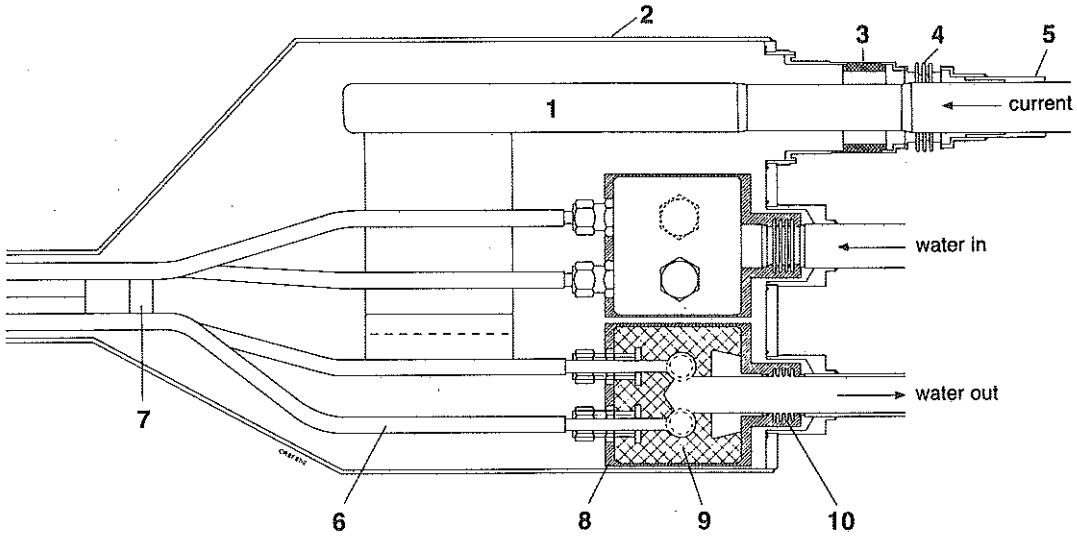

Figure 3b Can manifold and feedthrough housing. The current is led through (1) the can (2) separately from the water cooling through ceramic-metal seals (3). The water circuit is subdivided in eight hydraulically parallel circuits which are manifolded inside the can in order to reduce the risk of waterleak inside the vacuum. The manifold (9) is mechanically connected to the can by bellows (10) and surrounded by a silicon foam (8) to accommodate the shrinkage stress during curing.

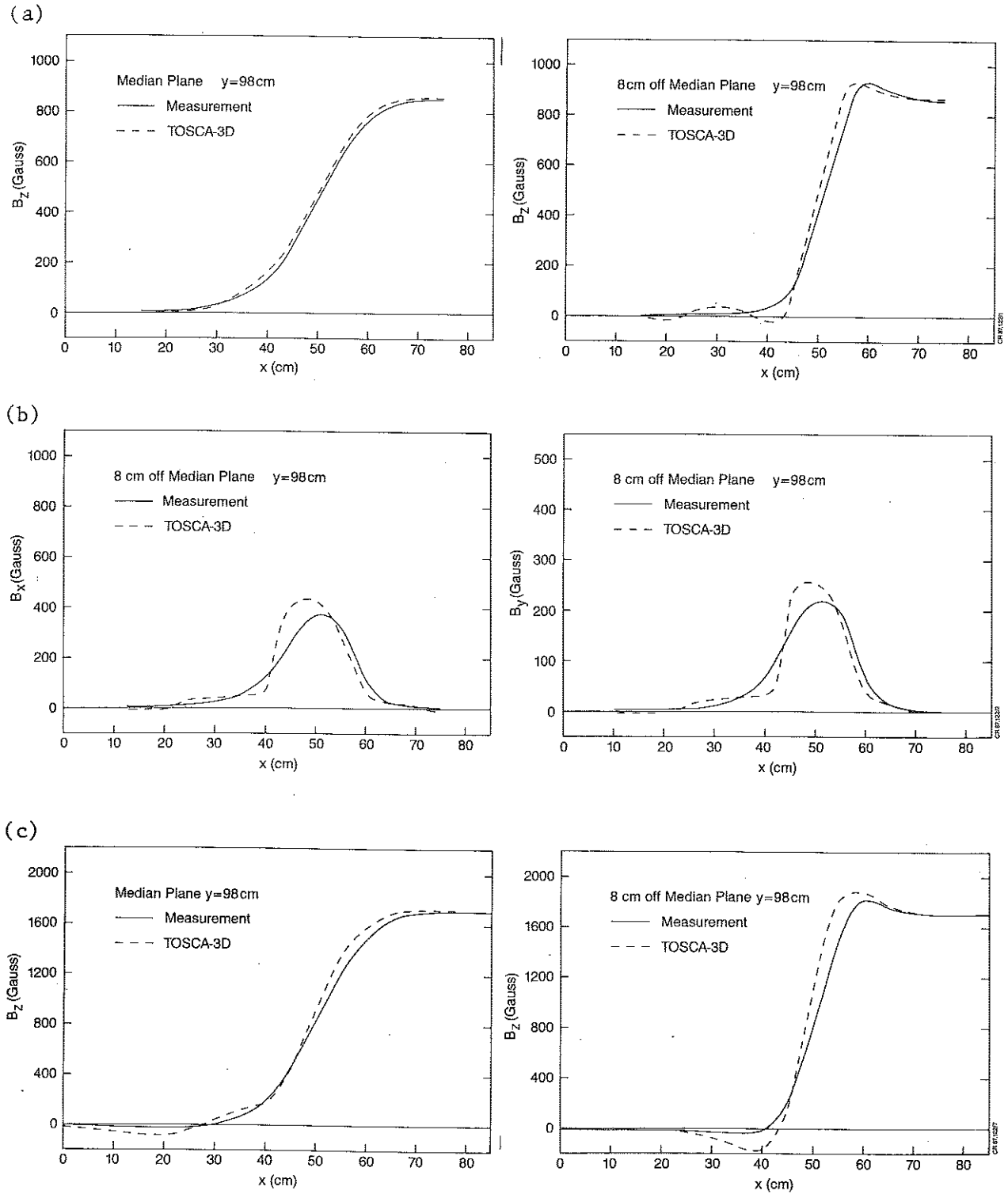

Figure 4a Comparison between measured and computed (TOSCA-3D) magnetic field (hydrogen operation mode). Shown on top is a plot of the field in the median plane (y = constant = 98 cm). The measured field integral is slightly lower (1.5% to 3.5%) than calculated which can be compensated by adjusting the magnet current. The bottom figure shows measured vs calculated magnetic field in a plane 8 cm off the median plane. Shown is the component perpendicular to the poleface. The measured fringe field is less steep than calculated resulting in a slightly weaker "vertical" focussing of the ion beams.

Figure 4b Magnetic field components parallel to the poleface in a plane 8 cm off the median plane, along the same chord as Figure 4a. The oscillation and the discreetness of the calculated profile is the most noticeable artefact in the computer result, but has a relatively small influence (5%) on the ion optics calculations.

Figure 4c Same as Figure 4a but at higher field excitation (deuterium operation mode). Iron saturation leading to field reversal is found to be less serious that calculated.